Article

Understanding Interfaces at the Positive and Negative Electrodes on Sulfide-Based Solid-State Batteries

Ander Orue Mendizabal, Manar Cheddadi, Artur Tron, Alexander Beutl, and Pedro López-Aranguren*

Cite This: *ACS Appl. Energy Mater.* 2023, 6, 11030−11042

Read Online

ACCESS		Metrics & More		Article Recommendations		Supporting Information

ABSTRACT: Despite the high ionic conductivity and attractive mechanical properties of sulfide-based solid-state batteries, this chemistry still faces key challenges to encompass fast rate and long cycling performance, mainly arising from dynamic and complex solid−solid interfaces. This work provides a comprehensive assessment of the cell performance-determining factors ascribed to the multiple sources of impedance from the individual processes taking place at the composite cathode with high-voltage $LiNi_{0.6}Mn_{0.2}Co_{0.2}O_2$, the sulfide argyrodite Li_6PS_5Cl separator, and the Li metal anode. From a multiconfigurational approach and an advanced deconvolution of electrochemical impedance signals

into distribution of relaxation times, we disentangle intricate underlying interfacial processes taking place at the battery components that play a major role on the overall performance. For the Li metal solid-state batteries, the cycling performance is highly sensitive to the chemomechanical properties of the cathode active material, formation of the SEI, and processes ascribed to Li diffusion in the cathode composite and in the space-charge layer. The outcomes of this work aim to facilitate the design of sulfide solid-state batteries and provide methodological inputs for battery aging assessment.

KEYWORDS: *sulfide electrolyte, solid-state battery, interface, electrode, chemomechanics, distribution of relaxation time*
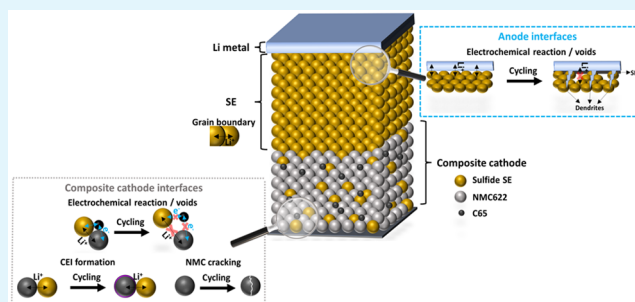
1. INTRODUCTION

The increasing demand for safe, highly efficient, and cost-effective energy storage systems has accelerated the development of solid-state batteries (SSBs) with lithium metal (LiM) anodes. This technology offers remarkable advantages over conventional lithium-ion batteries with liquid electrolytes, from improved safety with nonflammable electrolyte to higher gravimetric and volumetric energy density enabled using LiM anode along with the multilayered bipolar stacking cell fabrication. The combination of solid electrolyte (SE) mechanical strength, flexibility, and safety against self-ignition allows for optimized battery design to meet the specific requirements.[1−7]

Solid-state materials are characterized by a significant impact of interface-related phenomena on their functional character-istics such as mechanical properties, conductivity mechanisms, or electrochemical performance. For SSBs with ceramic or glass−ceramic electrolytes, the stacking of the composite cathode, the SE, and the LiM anode leads to multiple interfaces from voids, cracks, secondary phases from chemical and electrochemical reactions and grain boundaries.[8−11] As electrochemical kinetics is governed by the contact area at the interface, ensuring the adhesion between the electrolyte and active electrode materials is the key to obtaining high performance devices, especially at fast rates. In recent years, soft, flexible, and easily deformable sulfide-based electrolytes

have received significant attention due to their attractive mechanical properties, high conductivity, and feasibility of processing at ambient temperature, which makes them appealing candidates for upscaling the technology to large format devices.[2,5,12,13]

Sulfide-based materials have certain drawbacks related to their poor chemical stability toward ambient atmosphere and narrow electrochemical stability window.[6,7,14] For instance, the Li_6PS_5Cl (LPSCl) argyrodite phase exhibits thermodynamic stability in the potential range of 1.7−2.3 V vs Li/Li$^+$,[15] resulting in incompatibility between the electrolyte and Li metal anode or high-voltage $Li(Ni,Mn,Co)O_2$ (NMC) cathodes. Although in practice the stability window is generally larger for kinetic reasons or due to the formation of passivating layers,[16−18] there are numerous studies highlighting the reactivity at the sulfide/Li[19−21] or sulfide/NMC interface.[22−25] Additionally, mechanisms of degradation of sulfide-containing SSBs are ascribed to microstructural changes arising from the redox processes during cycling,[25−27] especially in the case of
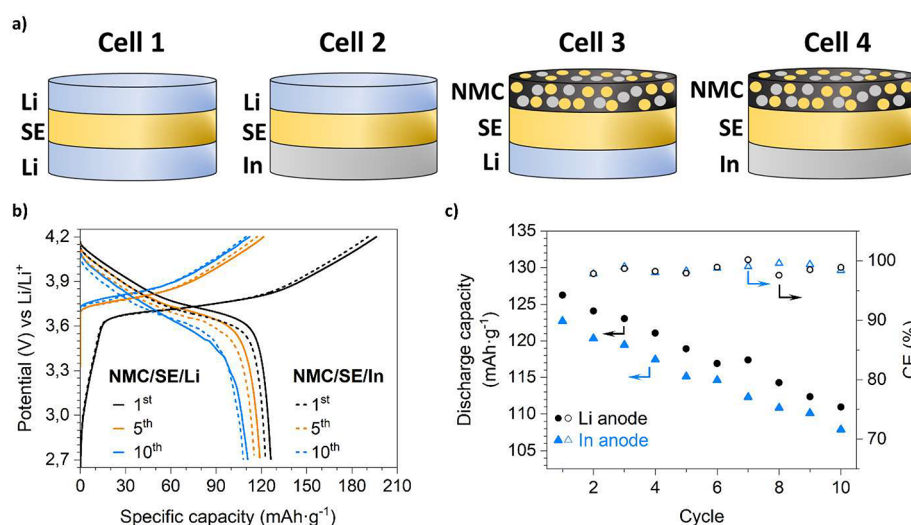
Figure 1. (a) Schematic illustration of Li/SE/Li (cell 1), Li/SE/In (cell 2), NMC/SE/Li (cell 3), and NMC/SE/In (cell 4) cell configurations. (b) Charge/discharge profiles and (c) discharge capacity and CE during the initial cycling of NMC/SE/Li and NMC/SE/In full cells.

large volume changes of the cathode active material upon delithiation,[23,27,28] poor percolation within the electron-conductive phase,[26] contact loss between the electrolyte and cathode or anode layers,[23,29−31] as well as dendrite propagation.[21,30]

Aging and degradation phenomena in SSBs can be comprehensively studied by electrochemical impedance spectroscopy (EIS), especially in the case of changes in the interfacial kinetics or conductivity mechanism of cell components. In combination with complementary characterization techniques, EIS can provide deep insights into the charge-transfer mechanisms within a cell or detect the origins of degradation.

The goal of the present work is to provide an understanding of the complex solid−solid interfaces regulating sulfide-based battery performance. Cells under different configurations with LPSCl, Li, or In metal anodes and $LiNi_{0.6}Mn_{0.2}Co_{0.2}O_2$ (NMC622)-based composite cathodes have been systematically studied aiming to bring insights on the dynamic interfaces at component level dominating processes during cell operation.

2. EXPERIMENTAL SECTION

LPSCl (NEI Corp., particle size (PS) 2−5 μm) was used as the SE for the fabrication of the cells. For the electrochemical testing of the SE, pellets of ∼700 μm thickness were prepared by densification of 30−35 mg of the electrolyte powder in a press-die of 6 mm diameter. The pressure was increased stepwise and maintained for 2 min at 300, 450, and 600 MPa. Symmetric cells with LiM anode (Li/SE/Li) were assembled using a Li foil of 6 mm diameter and a thickness of 200 μm (China Energy Lithium Co., Ltd.). Similarly, Li/SE/In cells were stacked using a 6 mm diameter and 100 μm thick Indium (In) foil (Sigma-Aldrich). A schematic illustration of symmetric cells is shown in Figure 1a.

For the fabrication of full cells, the composite cathode was prepared from the mixture of LPSCl, the cathode active material (CAM) $LiNi_{0.6}Mn_{0.2}Co_{0.2}O_2$ (NMC622, Targray, PS 10−30 μm), and carbon black (C65, TIMCAL) as conductive additive. The cathode components were mixed with a weight ratio of 28.2:67.4:4.4 (LPSCl:NMC622:C65) and ground in an agate mortar for 15 min. For the cell assembly, 30−35 mg of electrolyte powder was pressed (100−150 MPa); then, 4 mg of composite cathode was placed homogeneously distributed over the electrolyte surface and co-pressed with the electrolyte at 300−450−600 MPa holding 2 min at each pressure. The CAM loading was ∼1.6 mAh·cm$^{−2}$ and either Li or In

foil disks were used as a negative electrode. A schematic representation of the full cells is displayed in Figure 1a.

The electrochemical properties of the prepared cells were assessed in airtight in-house-made cells, with stainless steel plungers as current collectors. Stripping−plating tests were carried out on Li/SE/Li cells to investigate the reversibility of lithium deposition/dissolution and dendrite propagation. Combined with in situ galvanostatic electrochemical impedance spectroscopy (GEIS) analysis, these experiments allow simulation of the behavior of the electrolyte and Li/SE interface during galvanostatic cycling. The cycling was performed under the equivalent current density of C/20 for an areal capacity of 1.6 mAh·cm$^{−2}$. Each stripping or plating step lasted for 10 h while in situ GEIS analysis included 3 galvanostatic substeps of 3 h each, followed by EIS measurements (with 9.5−10 h of the total time of each step). A similar cycling procedure was applied for the Li/SE/In cell, including 5 galvanostatic substeps of 2 h.

Galvanostatic cycling of the full cells was performed under a current equivalent to C/20 in the voltage window of 2.7−4.2 V vs Li/Li$^+$, with a simultaneous periodic collection of EIS spectra in galvanostatic mode. The EIS spectra were collected in the range 1 MHz to 0.1 Hz, with 20−50 mV voltage amplitude. Although the collection of EIS data was performed during charging/discharging of the cell, the potential drift during a single EIS measurement was 5−10 times lower than the AC amplitude (at voltages above 3.5 V). Galvanostatic cycling and EIS measurements were conducted with a VMP3 potentiostat (BioLogic, France), whereas additional stripping−plating tests of Li/SE/Li cells were performed using a Neware battery tester.

The microstructure of the ceramic electrolyte, cathode layers, and SE/Li interface was studied by scanning electron microscopy (SEM) with a Quanta 200FEG electron microscope (Thermofischer) with an acceleration voltage of 10−20 kV collecting either secondary or backscattered electrodes. The cross-sectional micrographs of the electrolyte ceramics were acquired on fractured surfaces of a pellet. Top-view micrographs of the SE/Li interface on the stripped side were obtained after an electrochemical process for 10 h and subsequent removal of the partially delaminated Li metal layer. Microstructural changes in the composite cathode after cycling were assessed from top-view and cross-sectional SEM micrographs of the cathode side. For the cross section, the fractured surface was ion-milled by IM4000 (Hitachi) equipment using an airtight holder.

In order to achieve a higher resolution between overlapping process, distribution of relaxation times (DRT) analysis was applied to the results of EIS measurements using the DRTtools code based on Tikhonov regularization in MATLAB toolbox.[32,33] Nyquist-type plots were analyzed and fitted by using Z-view software. Kramer−Kronig
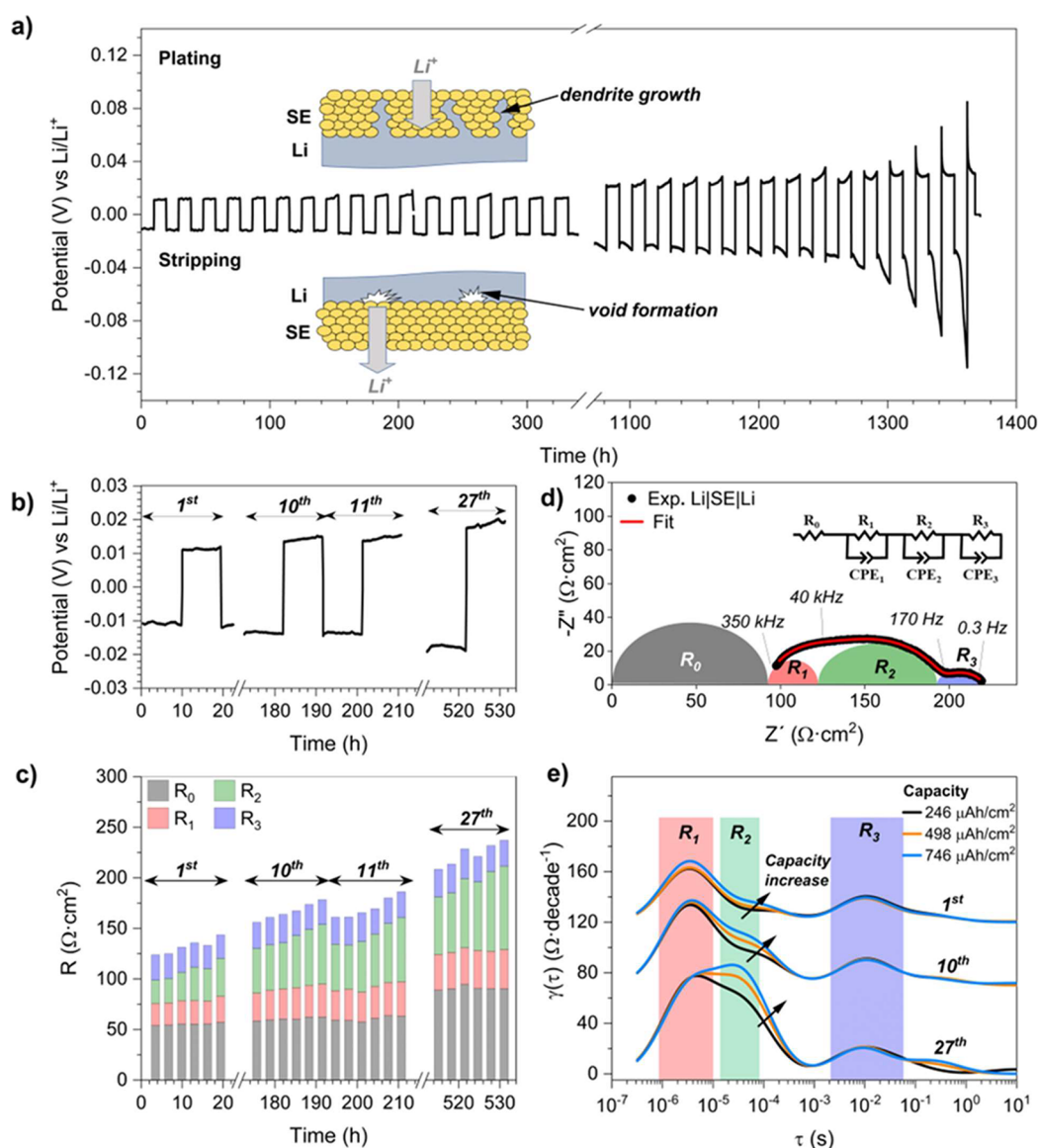
Figure 2. (a) Stripping–plating profile of a Li/SE/Li symmetrical cell at the current corresponding to C/20, (b) evolution of the cell potential, and (c) EIS components calculated with the EC method in accordance with the model presented in (d) equivalent circuit and fitting of the EIS of a Li symmetric cell. (e) DRT spectra calculated for the EIS data at the positive potentials at different amounts of stripped lithium during the 1st, 10th, and 27th cycles.

analysis was applied to validate the EIS measurements using the "Lin-KK" software developed by Karlsruhe Institute of Technology (KIT).[34] The residuals of the real and imaginary components of the EIS data are within the limit of 1%.[35,36]

3. RESULTS AND DISCUSSION

3.1. Electrochemical performance of full cells. Figure 1b illustrates the evolution of the initial 10 charge−discharge profiles for full cells assembled with Li or In anodes. The corresponding discharge capacity and Coulombic efficiency (CE) over cycling are plotted in Figure 1c. During the first cycle on the discharge step, both cells deliver about 64% of the initial charge of 190−200 mAh·g⁻¹. Both of them exhibit similar voltage profiles and a discharge capacity fading down to 110 mAh·g⁻¹, evidencing clear degradation occurring during cycling. The drop in performance during the first cycle is commonly attributed to the formation of a cathode electrolyte interphase (CEI) composed of the products resulting from the

interaction between argyrodite with the high-voltage cathode material.[22,23] Further cycling results in a gradual capacity loss of approximately 1.5% per cycle, with a CE remaining within the range of 98−100%.

The similar cycling behavior observed for both cells, in which only the LiM anode has been replaced by In, already suggests that there should be a relevant contribution from the charge transfer kinetics at the cathode/SE interface on the battery performance. The accurate identification of the dynamic processes occurring in the full cell is a challenging but necessary endeavor to improve the battery design. In this work, specific cell configurations have been designed to provide deeper insights into the processes taking place at both the anode/SE interface and within the cathode. First, a symmetric Li/SE/Li cell (labeled as cell 1 in Figure 1a) allows us to investigate in more details the kinetics of the lithium electrodeposition and electrodissolution from the Li/SE interface. Second, the asymmetric Li/SE/In cell (noted as

cell 2 in Figure 1a) brings additional information on the lithiation and delithiation of the Li−In negative alloy electrode. Finally, the results are confronted for the full cells NMC/SE/Li and NMC/SE/In (cells 3 and 4, respectively, in Figure 1a) aiming to identify the contribution of the NMC/SE interface to the overall impedance.

3.2. Stripping-plating of Li/SE/Li cell.

Figure 2a shows the voltage response of the Li/SE/Li symmetric cell after applying a constant current equivalent to C/20 for an areal capacity of 1.6 mAh·cm^{-2}, wherein the duration of each half cycle was 10 h (0.8 mAh cm^{-2}). The cell exhibits a stable cycling performance for more than 1300 h, with gradually increasing overpotential from 10 mV up to 30 mV (3−4% per cycle at the initial 1000 h). The voltage profile remains steady over 1100 h, evidencing a homogeneous stripping and plating of Li, and the cell continues cycling with increasing and fluctuating voltage. Indeed, the sudden voltage drop of the cell after around 1370 h, owed to dendrite propagation, drives the cell into short-circuit. It should be emphasized that despite the reduced time at each stripping−plating step with respect to the charge/discharge time of the full cells (10 h vs 15−20 h at C/20 current) and the low potential (several mV vs several V), the dendrite growth along other sources of degradation for the Li/SE/Li cell is quick to be formed at both sides, thus accelerating cell failure.[37] Therefore, the results of the stripping−plating test discussed in this section may be considered as relevant to the degradation rate taking place at the anode side of the full cells.

In situ GEIS analysis was performed at different cycling steps to understand the sources of impedance and the dynamic degradation processes on the overall resistance. The EIS measurements collected can be described accurately by the equivalent circuit (EC) model R$_0$-(RQ)$_1$-(RQ)$_2$-(RQ)$_3$ (Figure S1a-b), in accordance with the literature reporting symmetrical cells with a SE and reversible electrodes.[30,31,38] Table S1 compares the specific capacitance (C_i) for each individual (RQ)$_i$ component determined from the equivalent circuit model fitting of a symmetric Li/SE/Li cell.

The individual sources of impedance may be ascribed to different physical processes, thus leading to an ambiguous interpretation of EIS in the literature. In addition to this, the selection of an incorrect EC model may fall into large differences in the capacitance attributed to the same process. Identification of the observed EIS contribution can be performed using the values of the specific capacities of each RQ element (eqs S1 and S2) and comparing the calculated values with literature data reported for Li/Li$_6$PS$_5$Cl/Li cells. The specific capacitances calculated in our study are well in accordance with the respective parameters reported by Spencer-Jolly et al.[30] and Schlenker et al.[39] The noncapacitive element R_0 (the intercept at high-frequency with the real axis) can be attributed to the electrolyte bulk resistance,[31,39−41] whereas R_1 may correspond to the grain boundary (GB) resistance. The C_1 value calculated for the spectra in Figure S1a,b, is higher than the typical bulk/grain boundary capacitance (Table S1), likely due to more pronounced capacitive effects at the grain boundaries for the LPSCl. One should note that the grain boundary contribution is expected from the presence of well-defined grains in the microstructure of the cold-pressed SE observed by SEM analysis (Figure S1c). The calculation of the bulk and total (bulk + grain boundary) conductivity of LPSCl ceramics from the parameters R_0 and R_1 yields conductivities of 1.5 mS·cm^{-1} and 1.1 mS·cm^{-1},

respectively, at the start of the stripping−plating tests using eqs 1 and 2:

$$\sigma_{\text{bulk}} = \frac{l}{SR_0} \tag{1}$$

$$\sigma_{\text{bulk+GB}} = \frac{l}{S(R_0 + R_1)} \tag{2}$$

where l and S correspond to the sample thickness (cm) and area (cm^2).

Figure 2b,c shows the 1st, 10th, 11th, and 27th stripping−plating cycles and the corresponding evolution of the EIS elements determined by the EC model described in Figure 2d. The 10th and 11th cycles have been included in the analysis to understand the evolution of the elements on consecutive cycles. The components R_0 and R_1 display a similar increasing resistance of about 2.5% per cycle. The increase of R_1 may be due to microstructural changes in the densified electrolyte during cycling. Particularly, changes in the size of LPSCl particles due to interfacial reactions,[42] crack formation, and even pulverization of the electrolyte phase near the SE/Li interface have been previously observed.[43,44] A large increase in the grain boundary resistance has been reported for a cycled NMC811/LPSCl/Li-Si full cell.[45]

An additional aging mechanism of the electrolyte phase might involve the formation of insulating phases at the SE/Li interface. It is well-known that the argyrodite phase is thermodynamically unstable toward Li metal, and the contact between LPSCl and Li leads to the formation of solid electrolyte interphase (SEI) composed of resistive species such as Li$_3$P, Li$_2$S, and LiCl.[19,31] Processes ascribed to the SEI are observed at lower frequency and are characterized by a higher capacitance (Table S1) than the C_1 value calculated from our data. We explain this discrepancy from the accumulation of the SEI at the Li/SE interface which results in a decrease of the contact area and an increase of R_1, or the formation or propagation of the secondary phases along the GBs.[46] A particular case of the latter process is the deposition of Li metal at the grain boundaries leading to an increase in the R_1 component and accelerating the dendrite formation.[47]

The origin of increasing R_0 growth, and therefore a lower bulk conductivity, is the consequence of the structural decomposition of the argyrodite phase. It is known that the contact resistance may have an impact on the high-frequency EIS components;[10,30] in this case, the degradation might be associated with the contact loss between the electrodes and electrolyte due to SEI growth or mechanical issues that will be further discussed.

While R_0 and R_1 are essentially independent of the current direction and do not exhibit a clear trend during a single step, a different behavior is observed for the R_2 component (Figure 2c). As clearly shown in consecutive 10th and 11th cycles, keeping the cell under a fixed current leads to an increase of the total overpotential owed to a monotonous increase of the R_2 resistance. This process is especially pronounced when applying a positive current (Figure 2b), whereas on the subsequent negative current, R_2 decreases to the initial value. As observed from the 27th cycle, the resistance keeps increasing during cycling. R_2 seems to be the main component with an oscillating behavior as well as responsible for the overall increasing overpotential. The specific capacitance of R_2 (0.1−0.3 μF·cm^{-2}) approaches the common values for an SEI
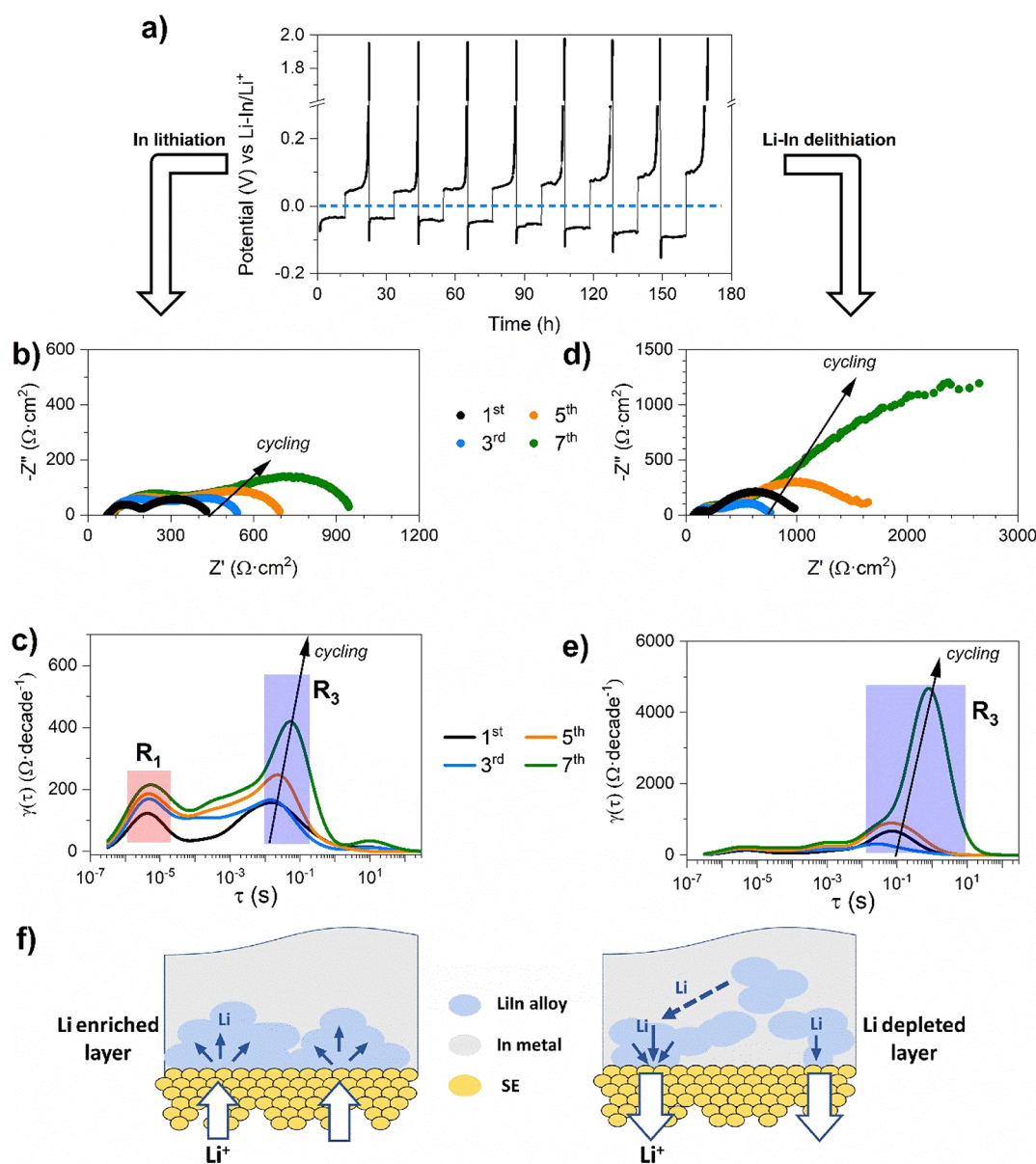
Figure 3. (a) Stripping-plating profile, (b, d) Nyquist plots, and (c, e) their corresponding DRT spectra collected in GEIS mode at the end of In lithiation or delithiation steps for a Li/SE/In cell. (f) Proposed scheme for the mechanism of intercalation and deintercalation of Li species into and from the Li−In electrode.

(Table S1). However, the oscillations observed for R_2 during cycling are not representative of the SEI. Particularly, the rapid drop of R_2 between the end of the 10th and the beginning of the 11th cycle indicates sudden drastic change at the interface, which is not consistent with slow processes of formation or dissolution of secondary phases. Therefore, another or additional process seems to be responsible for the trend observed on R_2. Recent studies of stripping−plating behavior with a 3-electrode cell revealed a significant increase in the overpotential at the stripping electrode, especially when a large amount of Li is removed.[30] This effect is attributed to void formation at the Li/SE interface, and as long as the constant current flows through the cell, more lithium is consumed close to the electrolyte surface, resulting in swelling of the voids and reduction of the contact area between the stripped electrode and electrolyte. After switching the current direction, Li deposition occurs inside the voids, and the overall over-

potential is maintained at a comparatively low level until void formation and growth occur at the opposite surface. One should note that the interpretation of the macroscopic physical processes on void formation would have been sluggish if only a 1D EC model is deemed. As reported by Eckhardt et al., a 3D electric network model can capture more accurately the effects of frequent-dependent current caused by current constrictions.[48,49] However, herein the void formation is resolved from the DRT analysis, which does not require prior knowledge of the system and allows us to deconvolute processes with close time constants.

We therefore suggest that the evolution of R_2, for which variations correlate with the current direction, arises from the periodic formation and healing of voids at the Li/SE interface. One should note that Spencer-Jolly et al.[30] attributed this resistance to the charge transfer phenomena, although there are no EIS data available to support this statement. In this

work, the specific capacity for $(RQ)_2$ is lower than could be expected for the charge transfer (Table S1). The trend observed in our work is supported by DRT, a powerful analysis method that allows discriminating the underlying electrochemical processes overlapping at similar frequencies on the EIS. Computing DRT involves the deconvolution of frequency-dependent EIS into a series of peaks with characteristic time-domain constants, corresponding to an individual rate-determining step.[10,50] Whereas the DRT peak with a characteristic relaxation time of $10^{-6}-10^{-5}$ s ($15-150$ kHz) is essentially constant within one step (Figure 2e), the shoulder at $10^{-5}-10^{-4}$ s indicates a periodic increase on each consecutive cycle, similar to the behavior observed for the R_2 component in Figure 2c. On the other hand, both peaks exhibit a significant increase after 27 cycles, stemming from a growing resistive SEI layer or reduction of the Li/SE contact area due to partial healing of Li voids.

There are no evident changes of R_3 and its respective DRT peak appearing at $\sim 10^{-2}$ s, neither during a single current step nor after multiple cycles (Figure 2c,e). The specific capacitance of the $(RQ)_3$ process (10^{-3} F·cm^{-2}) fits well with typical values of the charge-transfer process (Table S1). Since this is the lowest resistance among all, it indicates the fast kinetics of lithium electrodeposition and -dissolution from the SE/Li interface.

The comparison of the individual resistances in Figure 2c suggests that at the beginning of the cycling, the main source of impedance on the overall cell resistance is ascribed to the electrolyte bulk resistance (R_0) which amounts to almost 50% of the total resistance. Nevertheless, almost all of the resistances exhibit a growth after 27 cycles being especially pronounced for R_2. As discussed by Spencer-Jolly et al.,[30] the overpotential of the Li stripping step with a capacity of 0.8 mAh·cm^{-2} is approximately 2–5 times higher compared to the plating, although this ratio can be significantly affected by the pressure applied on the cell during cycling. Therefore, one could expect that for full cells, the contribution of the anode interface into the overall resistance should be more pronounced on discharge, i.e., on the Li stripping step at the negative electrode.

3.3. Li/SE/In cell. The results obtained for the Li/SE/Li cell indicate that the contact between Li and SE is critical for the electrochemical performance. It becomes meaningful to compare the interfaces from SE/Li and SE/In considering the different mechanisms between Li and In and Li electrodeposition as well as the lower ductility of Li−In compared with Li metal.

To understand the electrochemistry behind the LPSCl/In interface, stripping−plating in conjunction with GEIS was conducted on a Li/SE/In configuration (cell 2 in Figure 1a). The cell was assembled and cycled under a similar protocol as the symmetric Li/SE/Li cell, with 5 galvanostatic substeps of 2 h. Prior to cycling, the Li−In alloy was electrochemically formed by cycling the cell for 2 h, which generated an excessive amount of Li (~ 0.16 mAh·cm^{-2}) at the interface.

The stripping−plating profile for the Li/SE/In cell is shown in Figure 3a−c. The potential is normalized with respect to the Li−In/Li$^+$ potential (0.62 V). During the steps at negative current, corresponding to Li stripping from the Li metal side and the formation of the In−Li alloy at the In electrode (hereafter specified as "In lithiation"), the voltage shows a smooth profile and without significant fluctuations, indicating homogeneous electrochemical reactions at both electrodes

regardless of the current direction. One should note that the overpotential is higher compared to that for the Li/SE/Li cell (30 mV vs 11 mV at the first cycle) and increases during cycling to around 90 mV after 8 cycles, indicating that Li plating at the Li−In electrode is thermodynamically more hindered than the similar process at the pure Li surface.

On the reverse current (specified as "Li−In delithiation"), the overpotential at the earlier stage of the step is almost the same as for the opposite process but shows a rapid increase up to the voltage limit by the end of the step. This may indicate that at the early steps (i.e., for a low capacity), the kinetics of Li plating or stripping at the SE/Li−In electrode are similar, but for a higher capacity of In−Li delithiation, the significant increase of the overpotential is likely due to the Li shortage in the In−Li stoichiometry.

The stripping−plating voltage profile observed for a Li/SE/In cell is well in accordance with the EIS and DRT data collected within one cycle (Figure S2) or at the end of each lithiation (Figure 3b,c) and delithiation (Figure 3d,e) step. During a single step of In lithiation, there are no remarkable changes in the EIS spectra despite the slight decrease of the R_3 component (Figure S2a). However, the total impedance increases gradually from 400 Ω·cm^2 (1st cycle) to 1100 Ω·cm^2 (8th cycle), consistent with the slowly growing overpotential upon cycling. The increasing resistance mainly stems from R_1 and, especially R_3, whose effects are clearly seen in the evolution of the DRT spectra in Figure 3c. While the aging rate of the R_1 element is comparable to that for the Li/SE/Li cell (Figure 2c) and may be associated with similar microstructural changes or secondary phase formation from the Li-SE interaction, the evolution of R_3 upon cycling is particularly high for the Li/SE/In cell and deserves a more-in-depth discussion. A similar trend is observed for the In−Li delithiation step. Particularly, the R_3 component shows a substantial increase (up to 3 orders of magnitude) during a single In−Li delithiation step, especially at delithiation times of over 6 h (Figure S2c). A comparable difference was found between the end of the 1st and the 8th delithiation steps (Figure 3d). The onset of the rapid voltage growth on the delithiation steps shows a gradual shift toward shorter times on each consecutive cycle. For example, while for cycles 1−3, the overpotential was maintained at a nearly constant level up to 75−80% of the total step time, at the later cycles it dropped to 50%.

The frequency range of the RQ_3 element is generally ascribed to a charge-transfer process, which in fact may include several elementary processes, such as slow kinetics of the Li$^+$/ Li reduction or the thermodynamics of the Li−In alloy formation. One should note that a partial delamination of the electrodes on cycling, already observed in the Li/SE/Li cell (Figure S1d), could also be responsible for a decrease in the contact area available for the charge-transfer processes. However, if the latter factor had a significant influence on the charge-transfer resistance, a similar growth of R_3 would also be observed for the Li/SE/Li cell. As no substantial changes in the R_3 component for the Li/SE/Li cell were noticed on the EIS and DRT analysis (Figure 2c,e) despite the confirmed Li delamination, we can suggest that the charge-transfer processes are essentially not affected by the Li/SE contact area. Moreover, the degradation of the Li/SE contact due to void formation on Li stripping would lead to more pronounced differences in the EIS spectra during a single step than those depicted in Figure S1a,b.
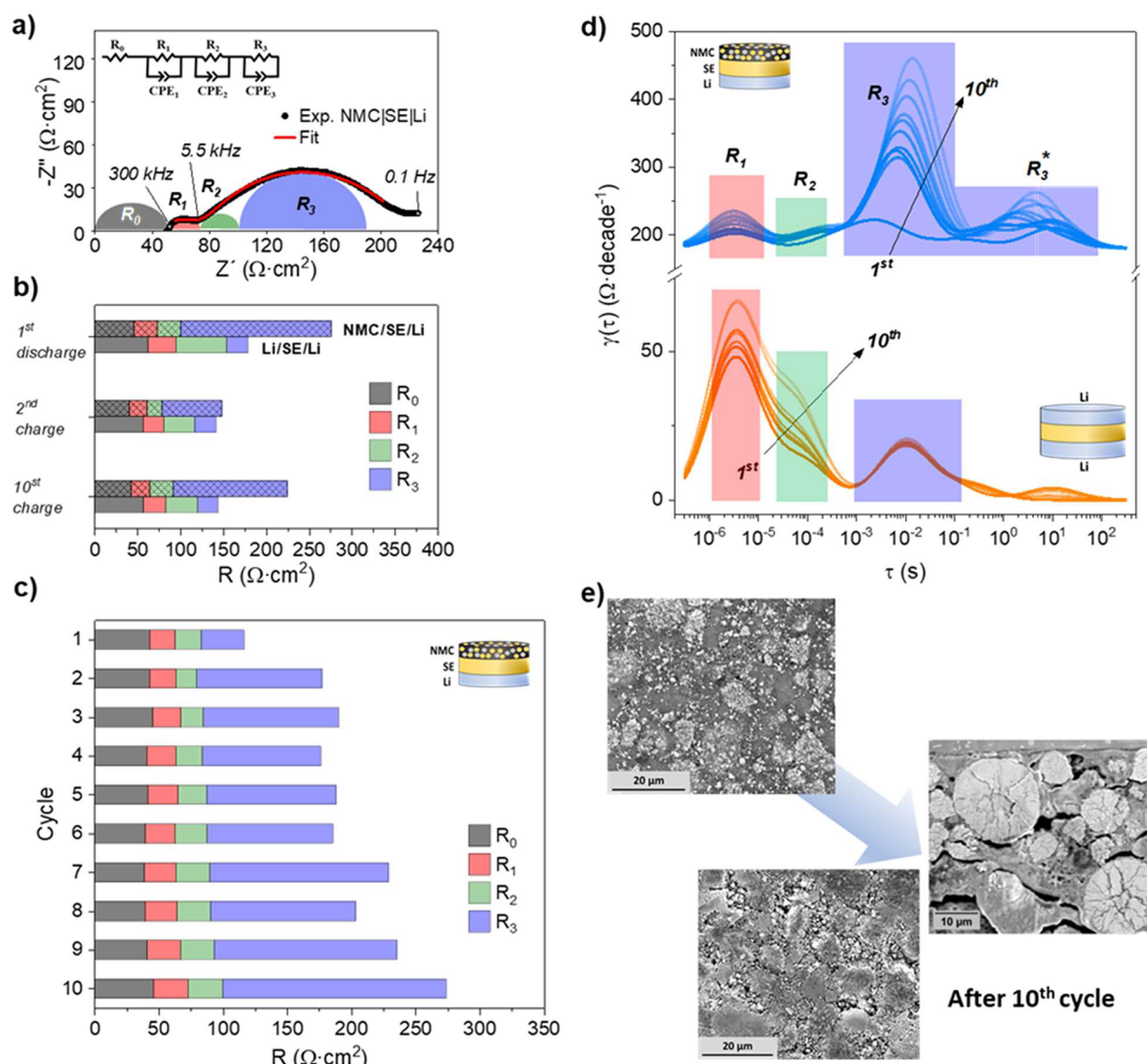
Figure 4. (a) Equivalent circuit and example of the fit for a typical EIS spectrum for NMC/SE/Li cell, (b) comparison of fit results for the Li/SE/Li and NMC/SE/Li cell collected at the 1st discharge, 2nd charge, and 10th charge at the amount of transferred Li of 750 μAh·cm^{-2}, (c) evolution of the fit parameters for NMC/SE/Li cell, (d) DRT spectra for NMC/SE/Li and Li/SE/Li cell on cycling, (e) comparison of the top-views on the NMC layer before and after 10 cycles and the cross-section micrograph of NMC cathode layer after cycling. For the Li/SE/Li cell, the charge and discharge steps correspond to the negative and positive currents in Figure 2a.

Li and In metals are known to form up to 7 intermetallic phases and respective solid solutions at room temperature.[51−54] During electrochemical lithiation of In, the Li content sequentially increases by the formation of the InLi phase that takes place at constant redox potential (0.62 V vs Li/Li$^+$).[54] The electrochemical lithiation of In by alloying is characterized by the negative formation enthalpy (−57 kJ mol^{-1}),[51,52] thus being thermodynamically favorable, especially at high In rich stoichiometry,[54] and has been reported up to a Li fraction of 60 atom % (In$_2$Li$_3$). The volume expansion for the InLi phase increases on Li incorporation by up to 53%, thus most likely improving the SE/Li−In contact during stripping and plating processes. Both the thermodynamic and kinetic factors of Li−In alloying are dependent on the homogeneity of the LiIn phase distribution within the interfacial and subinterfacial layers of the In electrode. Apparently, lithiation results in formation of LiIn alloy close to the interface and grows toward the In bulk onward, whereas during the delithiation step, the LiIn alloy interfacial layer

undergoes decomposition leading to formation of LiIn deposits in the electrode bulk isolated from the SE by the In layer (Figure 3f). Particularly, a similar mechanism supported by in situ scanning and transmission electron microscopy data was proposed by Wang et al.[55] During the delithiation process, the contact area between the LiIn alloy and SE decreases, whereas the thickness of the In layer separating the SE and LiIn domains in the electrode bulk grows, making the process of Li diffusion through In more critical. Both factors result in the insufficient rate of Li supply to the SE/Li−In interface which induces a large concentration overpotential, evidenced by an exceedingly large low-frequency semicircle in the Nyquist plots and high R_3 peaks in the DRT spectra (Figure S2d).

3.4. Comparison of symmetric vs full cells. Figure 4a shows the Nyquist plot of cell 3 (NMC/SE/Li). A detailed discussion of the EIS components and their evolution during the redox steps is given below. Primarily, one should highlight that both the full and symmetric Li/SE/Li cell can be adequately fitted by the similar EC model previously described,

although the respective contributions appear at a different frequency. For the NMC/SE/Li cell, the incipient tail at low frequency (<1 Hz) is likely ascribed to the Li^+ diffusion on the CAM particles.[40,56] The R_3 process appears partially overlapped with another low-frequency process. It has to be noted that the EC analysis may underestimate both of them due to the low-frequency tail contribution.

Previous EIS measurements for the Li/SE/Li cell (Figure 2c) confirmed that the overall impedance of the symmetric cell does not exceed 200–250 $\Omega \cdot cm^2$, with a significant contribution of the electrolyte bulk resistance (R_0) at the initial stages of cycling and a growing resistance R_2 associated with a partial delamination of the Li electrode during stripping-plating. Figure S3 shows a comparison of the Nyquist plots acquired for the full and symmetric cell on the 1st charge and 2nd and 10th discharge steps. The individual components R_0, R_1, R_2, and R_3, obtained from the spectra in Figure S3 using the EC models presented in Figure 2d and Figure 4a, are compared in Figure 4b. All the spectra were collected under the same current, equivalent to C/20, and time, after the beginning of the step (9.5 h, around 80 $mAh \cdot g^{-1}$). This ensures similar conditions of current density and electrochemically plated and stripped Li at the Li/SE interface for both symmetric and full cells. One should consider that the spectra obtained for the Li/SE/Li cell include the contribution from two Li/SE interfaces, whereas only one (stripping or plating electrode on the discharge or charge step, respectively) appears on the full cell. Therefore, one could expect overestimated resistances for the symmetric cells, especially when comparing with the full cell analyzed during charging, since in this case the EIS of Li/SE/Li is contributed by the stripping Li/SE interface with presumably higher interfacial resistance,[30,31,39] which is absent in the full cell case.

As observed in Figure 4b, the contribution of R_0 is slightly higher for the Li/SE/Li cell, despite using a SE with the same geometric dimensions in both cases. The co-pressing of the cathode and electrolyte layer may provide a better mechanical contact than the Li/SE interface leading to a lower R_0. The optimized contact at the cathode interface may also stem from the larger contact area achieved from the mixture of the SE and CAM powders, compared to the SE/Li interface, formed by stacking of the components. These suggestions are in agreement with a significant growth of R_0 observed for the Li/SE/Li cell after several cycles (Figure 2c).

From the available data, it is unclear if the $(RQ)_1$, $(RQ)_2$, and $(RQ)_3$ components for the symmetric cell correspond to the same processes for the NMC/SE/Li cell. The mechanism of Li stripping and plating at the anode is expected to be similar for the full and symmetric cell. Therefore, if any of the resistive components for the full cell is associated only with the anode, the specific capacitance of the respective RQ element is expected to be similar to that for the symmetric cell. Table S2 shows a comparison between the specific capacitances for the symmetric and full cell. One should note that the values of C_2 and C_3 for the Li/SE/Li cell are calculated for a single Li/SE interface, with the assumption that both stripping and plating interfaces provide the same contribution to the overall interfacial capacitance.

From Table S2, it follows that the components $(RQ)_1$ are characterized by capacitances of the same order ($\sim 10^{-9}$ F·cm^{-1}) for both cell configurations, whereas for the other elements, the respective capacitance differs by 2–3 orders. The EC model may not be accurate enough in the case of a large

overlap between the individual components, as is the case for R_2 and R_3 for the full cell. To discriminate between those processes and provide a more-in-depth comparison between the EIS data for the full and symmetric cell, the evolution of DRT spectra at different charge steps is presented in Figure 4d. The signals for both cells are within the same relaxation time for the $(RQ)_1$, $(RQ)_2$, and $(RQ)_3$ processes. Moreover, the intensity of the DRT peak for the $(RQ)_1$ signal, as well as the R_1 values in Figure 4b, are similar, within the uncertainties of the DRT and EC methods. This observation confirms that R_1 arises from grain boundary resistance of the SE, which is expected to be similar for the NMC/SE/Li and Li/SE/Li cells, as previously discussed. R_2 for the symmetric cell is twice of that of the full cell (Figure 4b), and DRT signals appear at similar time-domains (Figure 4d). This observation is well in accordance with the assignment of the $(RQ)_2$ element to the Li/SE interface (SEI + void formation), since in the case of the Li/SE/Li, this effect should be twice.

A large increase of the low-frequency arc (Figure 4b) and of the intensity of the DRT signal (Figure 4d) corresponding to the $(RQ)_3$ process is observed when the CAM/SE interface appears in the full cell. Moreover, an additional signal on the DRT of the full cells rises at high time-scale domains (marked as R_3^*) suggesting that the cathode interface brings additional diffusive processes with slow kinetics. R_3 and R_3^* contributions cannot be accurately calculated from the Nyquist plot due to the processes overlapping in the frequency domain in addition to the influence of the low-frequency tail. Considering the relaxation times for the R_3 (10^{-3}–10^{-1} s) and R_3^* (1–10 s) components which correspond to 2–200 Hz and 20–200 mHz in the frequency domain, respectively, the respective rate-limiting steps might be associated with diffusive processes at the cathode/SE interface.[23,41,56,57] However, further investigation is needed for a more accurate identification of the source of R_3 and R_3^*.

It is worth noting that the difference between the EIS and deconvoluted DRT of the symmetric and full cells becomes more pronounced during cycling. Particularly, during the initial cycles, the total impedance of the full cell is around 20% larger, whereas by the 10th cycle, this difference increases up to 50%. The most significant changes on cycling are observed for the R_1 and especially the R_3 component of the full cell, as can be observed in Figure 4c,d. As no obvious changes are found for the R_3 component of the Li/SE/Li cell after cycling (Figure 4d), the aging of the full cell should originate exclusively from the CAM/SE interface. Figure 4e illustrates a comparison of top-view SEM micrographs obtained for a pristine cathode surface and those after the 10th cycle. While the surface of the composite cathode before cycling is smooth and exhibits an intimate contact between the AM and SE particles, the cycling results in the modification of the microstructure by large void formation that leads to contact loss between particles. In addition, Figure 4e displays the ion-milled cross-section SEM micrograph of the composite cathode after cycling, where cracking of the NMC active material and the contact loss with the solid electrolyte are clearly noticeable. It is known that periodic delithiation and lithiation of NMC yield significant volume changes (4–5 vol % for NMC622), buildup of mechanical stresses in the crystal lattice of the cathode material, accompanied by its cracking, contact loss with the SE phase, resulting in performance drop.[23,27,28,58]

Comparison of the EIS at different cell potentials and after repeated cycling allows us to estimate the contribution of
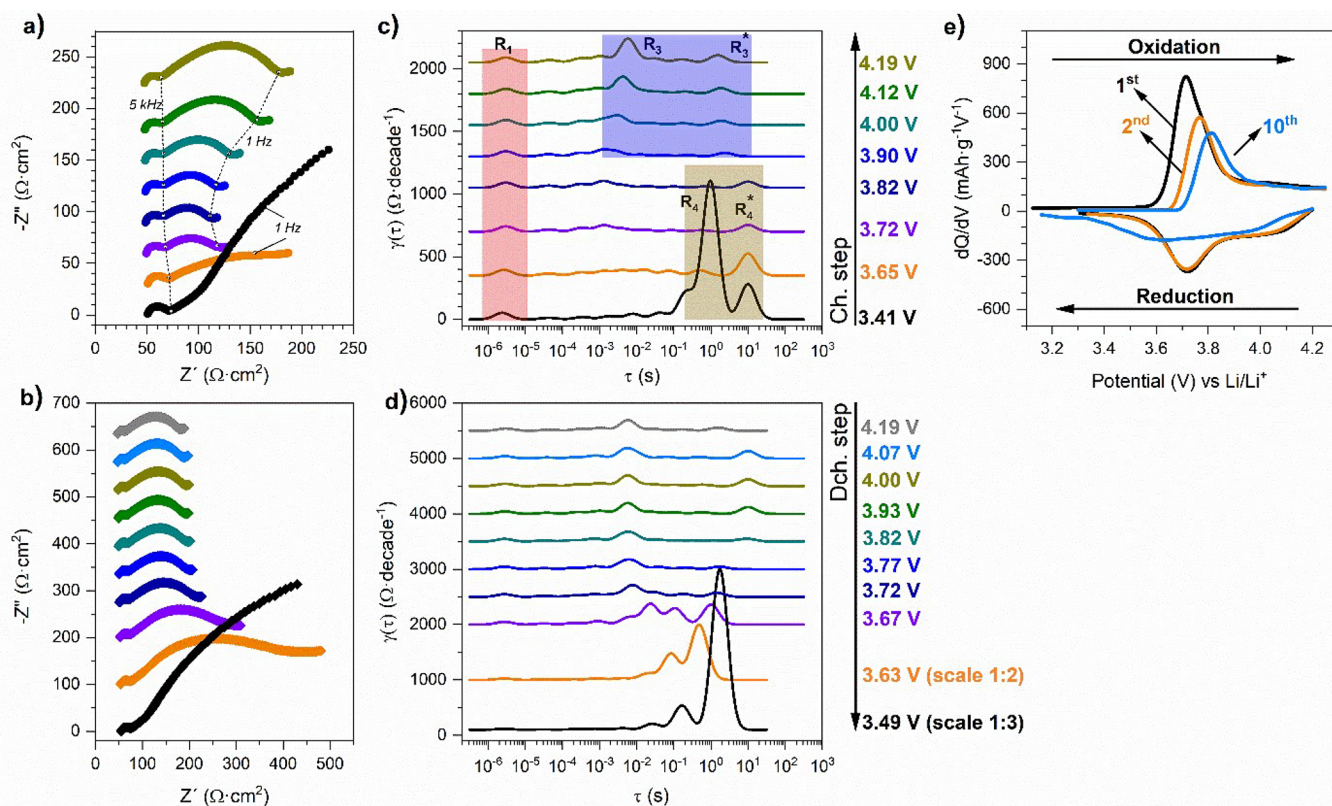
Figure 5. (a, b) Evolution of Nyquist plots collected in GEIS mode and (c, d) their corresponding DRT spectra during the 1st cycle of the NMC/SE/Li cell on the charge and discharge steps and (e) dQ/dV plots calculated for the 1st, 2nd, and 10th charge/discharge steps.
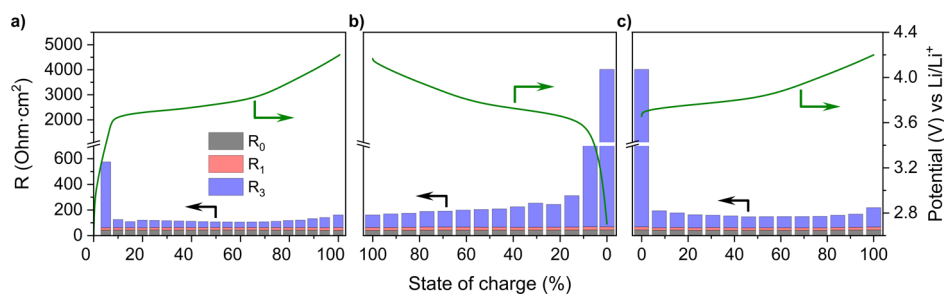
Figure 6. Evolution of the EIS fit parameters for the NMC/SE/Li full cell within (a) 1st charge, (b) 1st discharge, and (c) 2nd charge.

individual rate-determining steps to the overall degradation.[59,60] The evolution of Nyquist plots and corresponding DRT spectra for the full cell during the charge/discharge steps of the first cycle is summarized in Figure 5a−d, while the first charge and discharge curve obtained during the GEIS experiment is shown in Figure S4, and Table S3 lists the possible processes assigned to each component. The evolution of individual resistances R_0−R_3 during the initial cycles with the state of charge (SoC) of the cell is shown in Figure 6. Similar to what is observed in Figure 4c, the cell displays an increasing resistance during cycling.

The parameters R_0 and R_1 remain constant within the measurement/fitting errors during a single charge/discharge step. Assuming that these processes correspond to the electrolyte bulk and grain boundary resistance, it seems reasonable that the lithiation and delithiation of the active material do not have impact on these parameters. At longer cycling times, however, microstructural degradation or interaction between the components is expected to result in

more pronounced changes in the electrolyte properties or contact area between the cell components. R_3 is remarkably large at the initial SoC (Figure 6), i.e., at the cell potential below 3.5 V (start of charging or final period of discharge step). The corresponding DRT spectra (Figure 5c,d) displays large peaks at slow time-scale domains of 1 s (R_4) and 10 s (R_4^*). The cathode material in the discharged state introduces an additional resistance (much larger than the other contributions) into the total impedance, which rapidly decreases during the delithiation step. Previous calculations and experimental studies on the electrical properties of the CAM/SE interface have reported the presence of a space charge layer (SCL) associated with a nonhomogeneous charge distribution over the interface due to a large difference of the Li chemical potential between the cathode and electrolyte phase. In particular, DFT calculations for the $LiCoO_2/Li_3PS_4$ interface have revealed that during the initial delithiation, Li atoms start accumulating at the SE/CAM interface blocking the interfacial charge transfer and resulting in a large interfacial

resistance.[61] In situ HAAD-STEM investigation by Wang et al.[62] reported a redistribution of Li species over the $LiCoO_2$/LPSCl interface on changing the potential, which induces the appearance of an additional resistance. Based on these studies, as well as on the fact that the R_4 and R_4* peaks are present only for the discharged full cell, i.e., at high lithiation degree of the active material, we could tentatively ascribe these peaks to a SCL process.

At the intermediate stages of the voltage window (3.7−3.9 V), R_3 decreases to 20−25 $\Omega \cdot cm^2$ and increases on further charging. This voltage window is near the peak of the dQ/dV plot (~3.75 V vs Li/Li$^+$), displayed in Figure 5e, during the oxidation step. Further charging from 3.9 to 4.2 V results in a slight increase of the R_3 component (Figure 6) and of the DRT peaks at ~10^{-2} and 1 s (Figure 5c). Similar trends in the reverse order are observed on discharge with higher R_3 in comparison with the charging step at the same cell potentials.

It has been discussed in previous studies that the lithiation and delithiation of the active materials impact the transport properties of the active material. Besides the low-frequency Warburg-like tail,[38,40,63] a slow Li$^+$ diffusion in NMC can directly impact the charge transfer kinetics between the electrolyte and cathode phase, since the cathode reaction rate is determined by the supply of Li$^+$ toward the electrochemically active interface. The SCL properties, which are critical for cathode kinetics, can also be influenced by the CAM ionic conductivity. However, the information on the ionic conductivity in NMC-like materials is rather scattered and contradictive. Particularly, Cui et al.[64] and Wu et al.[65] have observed a gradual increase of the Li$^+$ diffusion coefficient on delithiation of $Li_{1-x}(Ni,Mn,Co)O_2$ (corresponding to the charge step of a full cell). Studies of Li transport in $LiNi_{0.4}Mn_{0.4}Co_{0.2}O_2$ from PEIS by Capron et al.[66] revealed a rapid increase of Li$^+$ diffusivity during charging and its subsequent stabilization at voltage above 3.8 V. In the study carried out by Charbonneau et al.,[67] the Li$^+$ diffusion coefficient in $LiNi_{1/3}Mn_{1/3}Co_{1/3}O_2$ exhibited a maximum value when the OCV of a full cell with the corresponding cathode achieves 3.9−4.3 V. The same voltage range corresponds to the lowest charge transfer resistance, suggesting that the electrochemical kinetics is determined by the cathode ionic conductivity.

The latter observation is in accordance with the low interfacial resistance between 3.8 and 4.0 V and its subsequent increase on further charging (Figure 5 and Figure 6). The shift of the voltage range corresponding to the minimum of R_3 compared to the data by Charbonneau et al.[67] might be explained by differences on the cathode formulation leading to a higher cell overpotential in the cited work. Regardless of this difference, the similar behavior in both cases indicates that the Li$^+$ diffusion coefficient in the cathode material is one of the factors responsible for the processes observed at intermediate frequency range.

4. CONCLUSIONS

The aim of this study was to investigate the governing factors determining performance and degradation mechanisms in SSBs from a comprehensive interfacial analysis by in situ galvanostatic EIS supported by DRT analysis. By comparing the results obtained from specific cell configurations during a single lithiation/delithiation step and multiple cycling, we elucidate the complex underlying and dynamic interfacial processes occurring at the cell components. The Li/SE interface experiences periodic void formation between the metallic anode and electrolyte, along with positive polarization applied to the respective electrode. This process leads to a loss of contact between the electrode and electrolyte, accompanied by an increase in the interfacial resistance during a single polarization step. Switching the cell polarity partially recovers the interface. Over the long term, the accumulation of interfacial defects results in significant detachment of the metal electrode and an irreversible increase of the cell overpotential. Some enhancement in grain boundary resistance is also observed, consistent with the microstructural aging of sulfide electrolyte. Nevertheless, these changes are minor compared to the performance losses caused by degradation of the SE/CAM interface, which involves the formation of interaction products between the NMC and LPSCl phases and morphological changes within the cathode layer. The results emphasize the importance of ensuring a tight contact between the SE and NMC or Li/In electrode, as well as the application of protective layers between the cathode and electrolyte phases.

The evolution of EIS and DRT spectra for the NMC/SE/Li full cell, in terms of cell potential, indicates a significant impact of the formation of a space charge layer (at a high lithiation degree) and Li diffusion in the cathode material (at a low lithiation degree) on the interfacial resistance. A more substantial effect of Li diffusion in Li−In on the interfacial resistance is observed for the Li/SE/In cell. Despite this effect, the performance of the NMC/SE/Li and NMC/SE/In full cells is quite similar, showing a comparable degradation rate. This confirms that the overall performance of the full cell is governed by the charge transfer across the CAM/SE interface. By diving into the fundamental factors determining performance at battery components, this work represents a useful guideline for the design and engineering of optimized interfaces in SSBs.

◼ ASSOCIATED CONTENT

Ⓢ Supporting Information

The Supporting Information is available free of charge at https://pubs.acs.org/doi/10.1021/acsaem.3c01894.

Nyquist plots obtained for a Li/SE/Li symmetrical cell in GEIS mode; cross-section SEM micrograph of an as-prepared fractured LSPCl ceramics; digital photo and top-view SEM micrograph of the SE/Li interface after 10 h of stripping and subsequent mechanical removal of Li electrode; Nyquist plots and their corresponding DRT spectra collected during the 8th cycle on In lithiation or delithiation steps for Li/SE/In cell; comparison of Nyquist plots collected for the Li/SE/Li and NMC/SE/Li cells in GEIS mode on the 1st charge, 2nd discharge, and 10th discharge steps; first charge−discharge curve obtained for NMC/SE/Li cell in GEIS mode; equations used to calculate the specific capacitance of each RQ component; comparison of specific capacitance values from different processes in symmetric Li/SE/Li cells; specific capacitances of the individual RQ elements for the symmetric Li/SE/Li and full NMC/SE/Li cell (PDF)

AUTHOR INFORMATION

Corresponding Author

Pedro López-Aranguren − *Center for Cooperative Research on Alternative Energies (CIC energiGUNE), Basque Research and Technology Alliance (BRTA), Parque Tecnológico de Álava, 01510 Vitoria-Gasteiz, Spain;* ◉ orcid.org/0000-0001-6912-2055; Email: plopez@cicenergigune.com

Authors

Ander Orue Mendizabal − *Center for Cooperative Research on Alternative Energies (CIC energiGUNE), Basque Research and Technology Alliance (BRTA), Parque Tecnológico de Álava, 01510 Vitoria-Gasteiz, Spain;* ◉ orcid.org/0000-0001-5802-4193

Manar Cheddadi − *Center for Cooperative Research on Alternative Energies (CIC energiGUNE), Basque Research and Technology Alliance (BRTA), Parque Tecnológico de Álava, 01510 Vitoria-Gasteiz, Spain*

Artur Tron − *Battery Technologies, Center for Low-Emission Transport, AIT Austrian Institute of Technology GmbH, 1210 Vienna, Austria;* ◉ orcid.org/0000-0002-6565-8247

Alexander Beutl − *Battery Technologies, Center for Low-Emission Transport, AIT Austrian Institute of Technology GmbH, 1210 Vienna, Austria*

Complete contact information is available at:
https://pubs.acs.org/10.1021/acsaem.3c01894

Author Contributions

Ander Orue: investigation, reviewing, validation, visualization, writing. Manar Cheddadi: investigation. Artur Tron: reviewing. Alexander Beutl: reviewing. Pedro López-Aranguren: conceptualization, funding acquisition, reviewing, supervision, visualization writing.

Notes

The authors declare no competing financial interest.

REFERENCES

(1) Zheng, F.; Kotobuki, M.; Song, S.; Lai, M. O.; Lu, L. Review on Solid Electrolytes for All-Solid-State Lithium-Ion Batteries. *J. Power Sources* **2018**, *389*, 198−213.

(2) Randau, S.; Weber, D. A.; Kötz, O.; Koerver, R.; Braun, P.; Weber, A.; Ivers-Tiffée, E.; Adermann, T.; Kulisch, J.; Zeier, W. G.; Richter, F. H.; Janek, J. Benchmarking the Performance of All-Solid-State Lithium Batteries. *Nat. Energy* **2020**, *5* (3), 259−270.

(3) Schnell, J.; Günther, T.; Knoche, T.; Vieider, C.; Köhler, L.; Just, A.; Keller, M.; Passerini, S.; Reinhart, G. All-Solid-State Lithium-Ion and Lithium Metal Batteries - Paving the Way to Large-Scale Production. *J. Power Sources* **2018**, *382*, 160−175.

(4) Lee, J.; Lee, T.; Char, K.; Kim, K. J.; Choi, J. W. Issues and Advances in Scaling up Sulfide-Based All-Solid-State Batteries. *Acc. Chem. Res.* **2021**, *54* (17), 3390−3402.

(5) Kim, K. J.; Balaish, M.; Wadaguchi, M.; Kong, L.; Rupp, J. L. M. Solid-State Li-Metal Batteries: Challenges and Horizons of Oxide and Sulfide Solid Electrolytes and Their Interfaces. *Adv. Energy Mater.* **2021**, *11* (1), 2002689.

(6) Tufail, M. K.; Zhai, P.; Khokar, W.; Jia, M.; Zhao, N.; Guo, X. Evaluation of Solid Electrolytes: Development of Conventional and Interdisciplinary Approaches. *Interdisciplinary Materials* **2023**, *2* (4), 529−568.

(7) Tufail, M. K.; Zhai, P.; Jia, M.; Zhao, N.; Guo, X. Design of Solid Electrolytes with Fast Ion Transport: Computation-Driven and Practical Approaches. *Energy Mater. Adv.* **2023**, *4*, 0015.

(8) Yu, S.; Siegel, D. J. Grain Boundary Contributions to Li-Ion Transport in the Solid Electrolyte $Li_7La_3Zr_2O_{12}$ (LLZO). *Chem. Mater.* **2017**, *29* (22), 9639−9647.

(9) Chen, R.; Li, Q.; Yu, X.; Chen, L.; Li, H. Approaching Practically Accessible Solid-State Batteries: Stability Issues Related to Solid Electrolytes and Interfaces. *Chem. Rev.* **2020**, *120* (14), 6820−6877.

(10) Pesci, F. M.; Bertei, A.; Brugge, R. H.; Emge, S. P.; Hekselman, A. K. O.; Marbella, L. E.; Grey, C. P.; Aguadero, A. Establishing Ultralow Activation Energies for Lithium Transport in Garnet Electrolytes. *ACS Appl. Mater. Interfaces* **2020**, *12* (29), 32806−32816.

(11) Banerjee, A.; Wang, X.; Fang, C.; Wu, E. A.; Meng, Y. S. Interfaces and Interphases in All-Solid-State Batteries with Inorganic Solid Electrolytes. *Chem. Rev.* **2020**, *120* (14), 6878−6933.

(12) Liu, S.; Zhou, L.; Han, J.; Wen, K.; Guan, S.; Xue, C.; Zhang, Z.; Xu, B.; Lin, Y.; Shen, Y.; Li, L.; Nan, C. Super Long-Cycling All-Solid-State Battery with Thin Li_6PS_5Cl-Based Electrolyte. *Adv. Energy Mater.* **2022**, *12* (25), 2200660.

(13) Batzer, M.; Heck, C.; Michalowski, P.; Kwade, A. Current Status of Formulations and Scalable Processes for Producing Sulfidic Solid-State Batteries. *Batteries Supercaps* **2022**, *5* (12), e202200328.

(14) Nikodimos, Y.; Huang, C.-J.; Taklu, B. W.; Su, W.-N.; Hwang, B. J. Chemical Stability of Sulfide Solid-State Electrolytes: Stability toward Humid Air and Compatibility with Solvents and Binders. *Energy Environ. Sci.* **2022**, *15* (3), 991−1033.

(15) Tan, D. H. S.; Wu, E. A.; Nguyen, H.; Chen, Z.; Marple, M. A. T.; Doux, J.-M.; Wang, X.; Yang, H.; Banerjee, A.; Meng, Y. S. Elucidating Reversible Electrochemical Redox of Li_6PS_5Cl Solid Electrolyte. *ACS Energy Lett.* **2019**, *4* (10), 2418−2427.

(16) Yu, C.; van Eijck, L.; Ganapathy, S.; Wagemaker, M. Synthesis, Structure and Electrochemical Performance of the Argyrodite Li 6 PS 5 Cl Solid Electrolyte for Li-Ion Solid State Batteries. *Electrochim. Acta* **2016**, *215*, 93−99.

(17) Zhang, Z.; Zhang, L.; Liu, Y.; Yu, C.; Yan, X.; Xu, B.; Wang, L. Synthesis and Characterization of Argyrodite Solid Electrolytes for All-Solid-State Li-Ion Batteries. *J. Alloys Compd.* **2018**, *747*, 227−235.

(18) Wang, S.; Zhang, Y.; Zhang, X.; Liu, T.; Lin, Y.-H.; Shen, Y.; Li, L.; Nan, C.-W. High-Conductivity Argyrodite Li_6PS_5Cl Solid Electrolytes Prepared via Optimized Sintering Processes for All-Solid-State Lithium-Sulfur Batteries. *ACS Appl. Mater. Interfaces* **2018**, *10* (49), 42279−42285.

(19) Wenzel, S.; Sedlmaier, S. J.; Dietrich, C.; Zeier, W. G.; Janek, J. Interfacial Reactivity and Interphase Growth of Argyrodite Solid Electrolytes at Lithium Metal Electrodes. *Solid State Ionics* **2018**, *318*, 102−112.

(20) Golov, A.; Carrasco, J. Molecular-Level Insight into the Interfacial Reactivity and Ionic Conductivity of a Li-Argyrodite Li_6PS_5Cl Solid Electrolyte at Bare and Coated Li-Metal Anodes. *ACS Appl. Mater. Interfaces* **2021**, *13* (36), 43734−43745.

(21) Liu, J.; Yuan, H.; Liu, H.; Zhao, C.; Lu, Y.; Cheng, X.; Huang, J.; Zhang, Q. Unlocking the Failure Mechanism of Solid State Lithium Metal Batteries. *Adv. Energy Mater.* **2022**, *12* (4), 2100748.

(22) Auvergniot, J.; Cassel, A.; Ledeuil, J.-B.; Viallet, V.; Seznec, V.; Dedryvère, R. Interface Stability of Argyrodite Li_6PS_5Cl toward $LiCoO_2$, $LiNi_{1/3}Co_{1/3}Mn_{1/3}O_2$, and $LiMn_2O_4$ in Bulk All-Solid-State Batteries. *Chem. Mater.* **2017**, *29* (9), 3883−3890.

(23) Koerver, R.; Aygun, I.; Leichtweiß, T.; Dietrich, C.; Zhang, W.; Binder, J. O.; Hartmann, P.; Zeier, W. G.; Janek, J. Capacity Fade in Solid-State Batteries: Interphase Formation and Chemo-Mechanical Processes in Nickel-Rich Layered Oxide Cathodes and Lithium Thiophosphate Solid Electrolytes. *Chem. Mater.* **2017**, *29* (13), 5574−5582.

(24) Wu, Y.-T.; Tsai, P.-C. Ab Initio Interfacial Chemical Stability of Argyrodite Sulfide Electrolytes and Layered-Structure Cathodes in Solid-State Lithium Batteries. *JOM* **2022**, *74* (12), 4664−4671.

(25) Deng, S.; Li, X.; Ren, Z.; Li, W.; Luo, J.; Liang, J.; Liang, J.; Banis, M. N.; Li, M.; Zhao, Y.; Li, X.; Wang, C.; Sun, Y.; Sun, Q.; Li, R.; Hu, Y.; Huang, H.; Zhang, L.; Lu, S.; Luo, J.; Sun, X. Dual-Functional Interfaces for Highly Stable Ni-Rich Layered Cathodes in Sulfide All-Solid-State Batteries. *Energy Storage Materials* 2020, 27, 117−123.

(26) Minnmann, P.; Strauss, F.; Bielefeld, A.; Ruess, R.; Adelhelm, P.; Burkhardt, S.; Dreyer, S. L.; Trevisanello, E.; Ehrenberg, H.; Brezesinski, T.; Richter, F. H.; Janek, J. Designing Cathodes and Cathode Active Materials for Solid-State Batteries. *Adv. Energy Mater.* 2022, 12 (35), 2201425.

(27) Bond, T.; Gauthier, R.; Gasilov, S.; Dahn, J. R. In-Situ Computed Tomography of Particle Microcracking and Electrode Damage in Cycled NMC622/Graphite Pouch Cell Batteries. *J. Electrochem. Soc.* 2022, 169 (8), 080531.

(28) Doerrer, C.; Capone, I.; Narayanan, S.; Liu, J.; Grovenor, C. R. M.; Pasta, M.; Grant, P. S. High Energy Density Single-Crystal NMC/ Li$_6$PS$_5$Cl Cathodes for All-Solid-State Lithium-Metal Batteries. *ACS Appl. Mater. Interfaces* 2021, 13 (31), 37809−37815.

(29) Deysher, G.; Ridley, P.; Ham, S.-Y.; Doux, J.-M.; Chen, Y.-T.; Wu, E. A.; Tan, D. H. S.; Cronk, A.; Jang, J.; Meng, Y. S. Transport and Mechanical Aspects of All-Solid-State Lithium Batteries. *Materials Today Physics* 2022, 24, 100679.

(30) Spencer-Jolly, D.; Ning, Z.; Hartley, G. O.; Liu, B.; Melvin, D. L. R.; Adamson, P.; Marrow, J.; Bruce, P. G. Temperature Dependence of Lithium Anode Voiding in Argyrodite Solid-State Batteries. *ACS Appl. Mater. Interfaces* 2021, 13 (19), 22708−22716.

(31) Narayanan, S.; Ulissi, U.; Gibson, J. S.; Chart, Y. A.; Weatherup, R. S.; Pasta, M. Effect of Current Density on the Solid Electrolyte Interphase Formation at the lithium|Li6PS5Cl Interface. *Nat. Commun.* 2022, 13 (1), 7237.

(32) Wan, T. H.; Saccoccio, M.; Chen, C.; Ciucci, F. Influence of the Discretization Methods on the Distribution of Relaxation Times Deconvolution: Implementing Radial Basis Functions with DRTtools. *Electrochim. Acta* 2015, 184, 483−499.

(33) Clematis, D.; Ferrari, T.; Bertei, A.; Asensio, A. M.; Carpanese, M. P.; Nicolella, C.; Barbucci, A. On the Stabilization and Extension of the Distribution of Relaxation Times Analysis. *Electrochim. Acta* 2021, 391, 138916.

(34) Schönleber, M.; Klotz, D.; Ivers-Tiffée, E. A Method for Improving the Robustness of Linear Kramers-Kronig Validity Tests. *Electrochim. Acta* 2014, 131, 20−27.

(35) Hahn, M.; Schindler, S.; Triebs, L.-C.; Danzer, M. A. Optimized Process Parameters for a Reproducible Distribution of Relaxation Times Analysis of Electrochemical Systems. *Batteries* 2019, 5 (2), 43.

(36) Soni, R.; Robinson, J. B.; Shearing, P. R.; Brett, D. J. L.; Rettie, A. J. E.; Miller, T. S. Lithium-Sulfur Battery Diagnostics through Distribution of Relaxation Times Analysis. *Energy Storage Materials* 2022, 51, 97−107.

(37) Ham, S.-Y.; Yang, H.; Nunez-cuacuas, O.; Tan, D. H. S.; Chen, Y.-T.; Deysher, G.; Cronk, A.; Ridley, P.; Doux, J.-M.; Wu, E. A.; Jang, J.; Meng, Y. S. Assessing the Critical Current Density of All-Solid-State Li Metal Symmetric and Full Cells. *Energy Storage Materials* 2023, 55, 455−462.

(38) Miß, V.; Ramanayagam, A.; Roling, B. Which Exchange Current Densities Can Be Achieved in Composite Cathodes of Bulk-Type All-Solid-State Batteries? A Comparative Case Study. *ACS Appl. Mater. Interfaces* 2022, 14 (33), 38246−38254.

(39) Schlenker, R.; Stępień, D.; Koch, P.; Hupfer, T.; Indris, S.; Roling, B.; Miß, V.; Fuchs, A.; Wilhelmi, M.; Ehrenberg, H. Understanding the Lifetime of Battery Cells Based on Solid-State Li$_6$PS$_5$Cl Electrolyte Paired with Lithium Metal Electrode. *ACS Appl. Mater. Interfaces* 2020, 12 (17), 20012−20025.

(40) Giraldo, S.; Nakagawa, K.; Vásquez, F. A.; Fujii, Y.; Wang, Y.; Miura, A.; Calderón, J. A.; Rosero-Navarro, N. C.; Tadanaga, K. Preparation of Composite Electrodes for All-Solid-State Batteries Based on Sulfide Electrolytes: An Electrochemical Point of View. *Batteries* 2021, 7 (4), 77.

(41) Choi, S.; Jeon, M.; Kim, B.-K.; Sang, B.-I.; Kim, H. Electrochemical Behaviors of Li-Argyrodite-Based All-Solid-State Batteries under Deep-Freezing Conditions. *Chem. Commun.* 2018, 54 (100), 14116−14119.

(42) Luo, S.; Wang, Z.; Li, X.; Liu, X.; Wang, H.; Ma, W.; Zhang, L.; Zhu, L.; Zhang, X. Growth of Lithium-Indium Dendrites in All-Solid-State Lithium-Based Batteries with Sulfide Electrolytes. *Nat. Commun.* 2021, 12 (1), 6968.

(43) Sheng, J.; Zhang, Q.; Liu, M.; Han, Z.; Li, C.; Sun, C.; Chen, B.; Zhong, X.; Qiu, L.; Zhou, G. Stabilized Solid Electrolyte Interphase Induced by Ultrathin Boron Nitride Membranes for Safe Lithium Metal Batteries. *Nano Lett.* 2021, 21 (19), 8447−8454.

(44) Zhao, Q.; Chen, X.; Hou, W.; Ye, B.; Zhang, Y.; Xia, X.; Wang, J. A Facile, Scalable, High Stability Lithium Metal Anode. *SusMat* 2022, 2 (1), 104−112.

(45) Jia, L.; Guo, B.; Zhang, X. Enabling Li$_{3.75}$Si Alloy Coupled with Argyrodite Electrolyte with Desirable Performance for All-Solid-State Batteries. *J. Phys.: Conf. Ser.* 2022, 2399 (1), 012012.

(46) Song, R.; Yao, J.; Xu, R.; Li, Z.; Yan, X.; Yu, C.; Huang, Z.; Zhang, L. Metastable Decomposition Realizing Dendrite-Free Solid-State Li Metal Batteries. *Adv. Energy Mater.* 2023, 13 (9), 2203631.

(47) Cao, D.; Zhang, Y.; Nolan, A. M.; Sun, X.; Liu, C.; Sheng, J.; Mo, Y.; Wang, Y.; Zhu, H. Stable Thiophosphate-Based All-Solid-State Lithium Batteries through Conformally Interfacial Nanocoating. *Nano Lett.* 2020, 20 (3), 1483−1490.

(48) Eckhardt, J. K.; Klar, P. J.; Janek, J.; Heiliger, C. Interplay of Dynamic Constriction and Interface Morphology between Reversible Metal Anode and Solid Electrolyte in Solid State Batteries. *ACS Appl. Mater. Interfaces* 2022, 14 (31), 35545−35554.

(49) Eckhardt, J. K.; Fuchs, T.; Burkhardt, S.; Klar, P. J.; Janek, J.; Heiliger, C. 3D Impedance Modeling of Metal Anodes in Solid-State Batteries-Incompatibility of Pore Formation and Constriction Effect in Physical-Based 1D Circuit Models. *ACS Appl. Mater. Interfaces* 2022, 14 (37), 42757−42769.

(50) Boukamp, B. A.; Macdonald, J. R. Alternatives to Kronig-Kramers transformation and testing, and estimation of distributions. *Solid State Ionics* 1994, 74, 85−101.

(51) Wen, C. J.; Huggins, R. A. Thermodynamic and mass transport properties of "LiIn". *Mater. Res. Bull.* 1980, 15, 1225−1234.

(52) Zhou, X.; Zhang, F.; Liu, S.; Du, Y.; Jin, B. Phase Equilibria and Thermodynamic Investigation of the In-Li System. *Calphad* 2020, 70, 101779.

(53) Qu, J.; Xiao, J.; Wang, T.; Legut, D.; Zhang, Q. High Rate Transfer Mechanism of Lithium Ions in Lithium-Tin and Lithium-Indium Alloys for Lithium Batteries. *J. Phys. Chem. C* 2020, 124 (45), 24644−24652.

(54) Santhosha, A. L.; Medenbach, L.; Buchheim, J. R.; Adelhelm, P. The Indium-Lithium Electrode in Solid-State Lithium-Ion Batteries: Phase Formation, Redox Potentials, and Interface Stability. *Batteries & Supercaps* 2019, 2 (6), 524−529.

(55) Wang, Z.; Zhao, J.; Zhang, X.; Rong, Z.; Tang, Y.; Liu, X.; Zhu, L.; Zhang, L.; Huang, J. Tailoring Lithium Concentration in Alloy Anodes for Long Cycling and High Areal Capacity in Sulfide-Based All Solid-State Batteries. *eScience* 2023, 3 (1), 100087.

(56) Zhang, Z.; Chen, S.; Yang, J.; Wang, J.; Yao, L.; Yao, X.; Cui, P.; Xu, X. Interface Re-Engineering of Li$_{10}$GeP$_2$S$_{12}$ Electrolyte and Lithium Anode for All-Solid-State Lithium Batteries with Ultralong Cycle Life. *ACS Appl. Mater. Interfaces* 2018, 10 (3), 2556−2565.

(57) Ruhl, J.; Riegger, L. M.; Ghidiu, M.; Zeier, W. G. Impact of Solvent Treatment of the Superionic Argyrodite Li$_6$PS$_5$Cl on Solid-State Battery Performance. *Adv. Energy Sustain Res.* 2021, 2 (2), 2000077.

(58) Spingler, F. B.; Kücher, S.; Phillips, R.; Moyassari, E.; Jossen, A. Electrochemically Stable In Situ Dilatometry of NMC, NCA and Graphite Electrodes for Lithium-Ion Cells Compared to XRD Measurements. *J. Electrochem. Soc.* 2021, 168 (4), 040515.

(59) Shrestha, S.; Kim, J.; Jeong, J.; Lee, H. J.; Kim, S. C.; Hah, H. J.; Oh, K.; Lee, S.-H. Effect of Amorphous LiPON Coating on Electrochemical Performance of LiNi$_{0.8}$Mn$_{0.1}$Co$_{0.1}$O$_2$

(NMC811) in All Solid-State Batteries. *J. Electrochem. Soc.* **2021**, *168* (6), 060537.

(60) Machida, N.; Kashiwagi, J.; Naito, M.; Shigematsu, T. Electrochemical Properties of All-Solid-State Batteries with ZrO2-Coated LiNi1/3Mn1/3Co1/3O2 as Cathode Materials. *Solid State Ionics* **2012**, *225*, 354−358.

(61) Haruyama, J.; Sodeyama, K.; Han, L.; Takada, K.; Tateyama, Y. Space-Charge Layer Effect at Interface between Oxide Cathode and Sulfide Electrolyte in All-Solid-State Lithium-Ion Battery. *Chem. Mater.* **2014**, *26* (14), 4248−4255.

(62) Wang, L.; Xie, R.; Chen, B.; Yu, X.; Ma, J.; Li, C.; Hu, Z.; Sun, X.; Xu, C.; Dong, S.; Chan, T.-S.; Luo, J.; Cui, G.; Chen, L. In-Situ Visualization of the Space-Charge-Layer Effect on Interfacial Lithium-Ion Transport in All-Solid-State Batteries. *Nat. Commun.* **2020**, *11* (1), 5889.

(63) Zhang, J.; Zheng, C.; Li, L.; Xia, Y.; Huang, H.; Gan, Y.; Liang, C.; He, X.; Tao, X.; Zhang, W. Unraveling the Intra and Intercycle Interfacial Evolution of Li $_6$ PS $_5$ Cl-Based All-Solid-State Lithium Batteries. *Adv. Energy Mater.* **2020**, *10* (4), 1903311.

(64) Cui, S.; Wei, Y.; Liu, T.; Deng, W.; Hu, Z.; Su, Y.; Li, H.; Li, M.; Guo, H.; Duan, Y.; Wang, W.; Rao, M.; Zheng, J.; Wang, X.; Pan, F. Optimized Temperature Effect of Li-Ion Diffusion with Layer Distance in Li(Ni $_x$ Mn $_y$ Co $_z$)O $_2$ Cathode Materials for High Performance Li-Ion Battery. *Adv. Energy Mater.* **2016**, *6* (4), 1501309.

(65) Wu, S.-L.; Zhang, W.; Song, X.; Shukla, A. K.; Liu, G.; Battaglia, V.; Srinivasan, V. High Rate Capability of Li(Ni $_{1/3}$ Mn $_{1/3}$ Co $_{1/3}$)O $_2$ Electrode for Li-Ion Batteries. *J. Electrochem. Soc.* **2012**, *159* (4), A438−A444.

(66) Capron, O.; Gopalakrishnan, R.; Jaguemont, J.; Van Den Bossche, P.; Omar, N.; Van Mierlo, J. On the Ageing of High Energy Lithium-Ion Batteries—Comprehensive Electrochemical Diffusivity Studies of Harvested Nickel Manganese Cobalt Electrodes. *Materials* **2018**, *11* (2), 176.

(67) Charbonneau, V.; Lasia, A.; Brisard, G. Impedance Studies of Li + Diffusion in Nickel Manganese Cobalt Oxide (NMC) during Charge/Discharge Cycles. *J. Electroanal. Chem.* **2020**, *875*, 113944.